Heating-frequency-dependent thermal conductivity: An analytical solution from diffusive to ballistic regime and its relevance to phonon scattering measurements

Fan Yang and Chris Dames[*]

Department of Mechanical Engineering, University of California at Berkeley, Berkeley, California 94720, USA
and Materials Sciences Division, Lawrence Berkeley National Laboratory, Berkeley, California 94720, USA

The heating-frequency dependence of the apparent thermal conductivity in a semi-infinite body with periodic planar surface heating is explained by an analytical solution to the Boltzmann transport equation. This solution is obtained using a two-flux model and gray mean free time approximation and verified numerically with a lattice Boltzmann method and numerical results from the literature. Extending the gray solution to the nongray regime leads to an integral transform and accumulation-function representation of the phonon scattering spectrum, where the natural variable is mean free time rather than mean free path, as often used in previous work. The derivation leads to an approximate cutoff conduction similar in spirit to that of Koh and Cahill [Phys. Rev. B **76**, 075207 (2007)] except that the most appropriate criterion involves the heater frequency rather than thermal diffusion length. The nongray calculations are consistent with Koh and Cahill's experimental observation that the apparent thermal conductivity shows a stronger heater-frequency dependence in a SiGe alloy than in natural Si. Finally these results are demonstrated using a virtual experiment, which fits the phase lag between surface temperature and heat flux to obtain the apparent thermal conductivity and accumulation function.

I. INTRODUCTION

The diffusion process of Fourier's law of heat conduction breaks down whenever the characteristic length or timescale of a problem is smaller than the energy carrier's mean free path (MFP) or mean free time (MFT, i.e., relaxation time), respectively. Understanding the corresponding MFP or MFT distributions is crucial for understanding the thermal conductivity in nanostructured materials [1] or ultrafast process [2–4] and thus would help in designing and optimizing a wide range of applications, such as heat dissipation and chip cooling [5,6], thermoelectric energy conversion [7,8], and nanomedicine [9]. All studies of the thermal conductivity accumulation function to date have used MFP as the independent variable of the accumulation, including both modeling [1,10–15] and experiments [2,16–19].

One approach to measuring the accumulation function is by varying the size of a small heat source to restrict the range of phonons that can fully participate in the heat conduction. In this way, Minnich *et al.* [16,20] reported direct measurements of the phonon accumulation function using optical heat sources with sizes first in the range of tens of microns, then tens of nanometers [21]. Based on a related steady-state solution to the Boltzmann transport equation (BTE) [22], a cutoff approximation was made that phonons with MFPs larger than the spot size were fully ballistic and contributed negligibly to heat conduction. Thus, the measured apparent thermal conductivity was taken to represent the contribution of the phonons with MFP less than the spot size.

The other method used to obtain the accumulation function is by varying the heating frequency. Koh and Cahill [2] first measured heating-frequency-dependent thermal conductivity and reported the thermal conductivity per MFP, the derivative of the accumulation function. For several semiconductor alloys, they found that the thermal conductivity measured by time domain thermoreflectance (TDTR) depended on heating frequency even at frequencies below 10 MHz. Similar measurements were extended to higher heating frequency (200 MHz) by Regner *et al.* [18] using frequency domain thermoreflectance (FDTR). In both approaches, the thermal conductivity accumulation function was calculated using Koh and Cahill's cutoff assumption that phonons with MFPs longer than the Fourier-law penetration depth would not conduct heat, evaluated using either the bulk [2] or frequency-dependent [18] thermal diffusivity.

This approach of using some form of truncated Fourier law is very common in the accumulation measurements and data interpretation [2,16–18,23,24]. Since these experiments are specifically designed so that nondiffusive effects are significant over much of the measurement range, the question arises whether the Fourier law is an appropriate treatment for these measurements. A quantitative assessment of Koh and Cahill's cutoff assumption [2] by comparison with a more rigorous analysis is still needed. Thus, nondiffusive solutions to the BTE have attracted great attention recently. There are numerical efforts on solving the BTE to obtain the accumulation function [20,25,26]. Most recently, to deeply understand the nondiffusive transport, there are also reports on analytical solutions. Collins *et al.* [27] and Hua and Minnich [28] analytically solved the BTE for transient thermal grating. Regner *et al.* [29] obtained analytical solutions to the BTE for time-periodic surface heating in both planar and spherical geometries. They applied this solution to investigate the effects of penetration depth and heating source size, as well as the suppression function.

For such periodic heating experiments, an important research topic is developing more rigorous analytical tools to relate the measured macroscopic properties to the fundamental microscopic properties. For example, in FDTR [18] the goal is to use the measured phase lag between surface temperature and heat flux to obtain a phonon accumulation function. An

_____
[*]Corresponding author: cdames@berkeley.edu
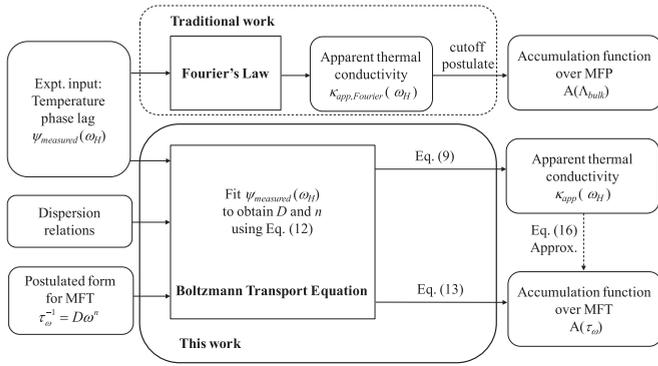
FIG. 1. Conceptual comparison between Fourier (traditional) (Ref. [18]) and BTE (this work) approaches for obtaining the phonon accumulation function from measured temperature phase lag data in FDTR.

FIG. 2. (Color online) Schematic of two-flux BTE model of a semi-infinite solid with a planar periodic heat source of angular frequency ω_H. The distribution of equilibrium BTE temperature (solid purple line) is depicted for one instant in time as well the envelope of its amplitude (dashed black line).

additional challenge in the extraction of accumulation functions from some TDTR [2,16] or FDTR [18] experiments is that the measurements potentially involve subcontinuum phenomena in both timescale (modulation frequency) and lengthscale (laser spot size). Isolating the effects of each mechanism also needs to be explored. For steady-state problems where only lengthscales matter, rigorous BTE solutions are known and yield a Fredholm integral equation that connects measurements to a MFP-based accumulation function [15,26]. Here, we consider the complementary case where the subcontinuum phenomena arise purely from a periodic timescale effect by using an infinite plane source to eliminate any spot size effects.

Below, we build up a BTE-based framework to interpret the experimental quantities and bridge them to the nondiffusive properties, as shown in Fig. 1. We first obtain an analytical solution to the gray BTE with a planar heat source [29]. Then, we extend this gray model to the nongray regime, which helps explain the heating-frequency-dependent thermal conductivity observed for semiconductor alloys [2]. Next we present a scheme by which transient measurements can be analyzed using the BTE rather than Fourier's law, summarized in Fig. 1 and discussed in Sec. II C. Finally, a virtual experiment is considered. For periodic planar heating, the results show that the phonon accumulation function is more appropriately expressed with respect to MFT than MFP; similarly, if a cutoff approximation is used in analyzing the measurements, it is more appropriate to use the heater timescale directly rather than the corresponding Fourier-law penetration depth.

II. DESCRIPTION OF MODEL

For brevity, here we present the problem statement, outline the solution, and give the key theoretical results. Derivation details are deferred to the Appendices, including the two-flux BTE (Appendix A); solutions for temperature, heat flux, penetration depth, and phase lag (Appendix B); the relationship between effective carrier velocities in one-dimensional (1D) and three-dimensional (3D) models (Appendix C); and the solution using the 3D velocity treatment (Appendix D).
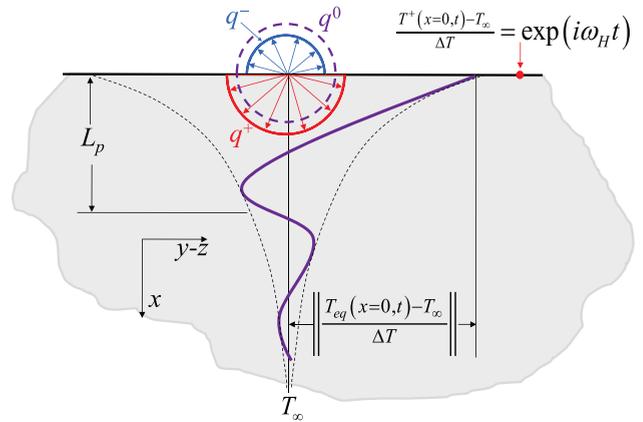
A. Periodic heating problem and BTE

We consider heat conduction in a semi-infinite solid with periodic plane-source heating on the surface, including the case where the heating frequency is high enough that nondiffusive effects cannot be neglected. In current TDTR and FDTR experiments, the fastest heating frequencies ($\sim$10 to 200 MHz [2,17,18]) are still several orders of magnitude smaller than typical semiconductor phonon vibrational frequencies ω. Thus, quantum wave effects should be negligible and phonon wave packets can be treated as particles, so that the BTE is applicable [30].

We start from the transient 3D BTE, which is complicated and time consuming to solve for an arbitrary geometry. However, as indicated in Fig. 2, the present problem is greatly simplified. The translational symmetry of the planar heating eliminates the y and z spatial coordinates from consideration. The two-flux treatment, which assumes isotropic phonon intensities over the forward and backward hemispheres but with two different amplitudes [31], greatly simplifies the wave vector dependence. Furthermore, the time dependence is simply steady-periodic in response to the heater frequency ω_H.

Taking full advantage of the 1D nature of the transport depicted in Fig. 2 involves some modeling subtleties. For details, see Appendix D. In general, the group velocity for a single polarization depends on the phonon frequency and direction: $\mathbf{v} = \mathbf{v}(\omega, \theta, \phi)$, where θ is the polar angle measured from the x axis and ϕ is the azimuthal angle. Due to the symmetries and material isotropy of our problem, there clearly is no ϕ dependence. To further simplify the θ dependence, we use a two-flux approach, which is common in the radiation literature [31] and is detailed in Appendix A. Within a two-flux approximation, there are still two slightly different ways to treat the group velocity vectors. For transient modeling, the most common treatment [18,32] [Fig. 3(a)] approximates all group velocity vectors as lying purely in the $+\hat{\mathbf{x}}$ or $-\hat{\mathbf{x}}$ directions, with a speed $v_{1D}(\omega)$. A more realistic Schuster-Schwarzschild or Milne-Eddington approach [31] [Fig. 3(b)] uses an isotropic dispersion relation where all phonons of a
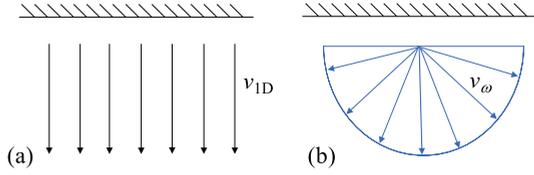
FIG. 3. (Color online) Two different implementations of the two-flux model of phonon radiation, as applied to the nominally 1D problem of Fig. 2. (a) Phonons can travel only in the $\pm \hat{\mathbf{x}}$ directions. (b) Phonons travel isotropically with speed v_ω, while the net transport remains 1D along $\pm \hat{\mathbf{x}}$.

given frequency share the same speed v_ω. Below, we first develop the BTE solution using the scheme of Fig. 3(a) and verify it using a numerical lattice BTE (LBTE) method, followed by extension to the scheme of Fig. 3(b).

The BTE solutions in the Appendices A and B are first solved using a gray approximation, whereby all phonons have the same MFT. Then, to allow for materials where the phonons have a broad distribution of MFTs [1,10,15,16,18], the solution is extended to the nongray regime in Sec. II B using a similar method as Ref. [33]. In both cases we use an isotropic Born–von Karman (BvK) dispersion with a Slack-like Umklapp scattering law (BvKS model) [33]. Optical modes are neglected due to their small group velocity; since this also neglects their potential role as a thermal reservoir, it is only appropriate below the corresponding Einstein temperatures [32,34]. We lump the three acoustic polarizations into a single branch, a common approximation [15,32,35,36], which has previously been shown to give good agreement with experiments for both bulk [37] and nanowires [35].

In the single mode relaxation time approximation, the BTE has the form [38,39]

$$\frac{\partial f_\omega}{\partial t} + v_\omega \mu \frac{\partial f_\omega}{\partial x} = \frac{f_\omega^0 - f_\omega}{\tau_\omega}, \tag{1}$$

where f_ω is the distribution function, f_ω^0 is the equilibrium distribution function, v_ω is the magnitude of the group velocity, $\mu = \cos\theta$ is the direction cosine, τ_ω is the MFT, and the subscript ω indicates quantities that depend on ω. In the first scheme of Fig. 3(a), $\mu = \pm 1 = $ constant. We have also performed the derivation following the more general scheme of Fig. 3(b), with key results given in Appendix D.

As exemplified by FDTR [18,40], an important class of experiments is based on the periodic surface heating of a semi-infinite material, which obviously causes the surface temperature to fluctuate at the same frequency, ω_H. For mathematical convenience, we prefer to solve the BTE using surface temperature as the forcing and thus the surface heat flux is the response. Since the solution is unique, once the relationship between temperature and flux is found, the solution applies just as well to the experimental situation. Specifically, we choose to force the two-flux problem using the boundary condition

$$T^+(x = 0, t) = T_\infty + \Delta T \exp(i\omega_H t), \tag{2}$$

where the superscript "$+$" means forward direction (later the superscript "$-$" means backward direction), T_∞ is the ambient temperature, and $\Delta T \ll T_\infty$ is the amplitude of the

T^+ oscillation. Building on this boundary condition, the BTE of Eq. (1) can be solved for the gray two-flux model, as detailed in Appendices A and B. The key results are the equilibrium temperature T_{eq} and surface heat flux $q_{net}^{''}$, given in Eqs. (B3) and (B6), respectively.

B. Apparent thermal conductivity: gray and nongray model

We define an apparent thermal conductivity using the ratio of heat flux to equilibrium temperature gradient,

$$k_{app,gray}(\omega_H) = \left\| \frac{q_{net}^{''}(\omega_H, x, t)}{-\frac{\partial T_{eq}(x,t)}{\partial x}} \right\|. \tag{3}$$

Reassuringly, in the detailed solutions of $q_{net}^{''}(\omega_H, x, t)$ and $T_{eq}(x,t)$, we find that the dependencies on x and t appear in exactly the same form and thus cancel out of $k_{app,gray}$. Clearly, the definition in Eq. (3) simply approaches the bulk value $k_{Fourier}$ whenever Fourier's law of heat conduction holds. Substituting the relevant results from Appendix B, we find

$$k_{app,gray}(\omega_H) = B_t(\omega_H \tau_{gray}) k_{Fourier}, \tag{4}$$

where τ_{gray} is the gray MFT and $B_t(\omega_H \tau_{gray})$ captures the subcontinuum effects of periodic heating and is found to be

$$B_t(\omega_H \tau_{gray}) = \sqrt{\frac{1 + d^2 - 2d\cos\phi}{1 + d^2 + 2d\cos\phi}} \frac{1}{\sqrt{a^2 + b^2}}. \tag{5}$$

Here a, b, ϕ, and d themselves are functions only of $\omega_H \tau_{gray}$ and are defined and explained in Appendix A. The B_t function is plotted in Fig. 4(a). For $\omega_H \tau_{gray} \ll 1$, $B_t(\omega_H \tau_{gray}) \to 1$, correctly recovering the Fourier limit.
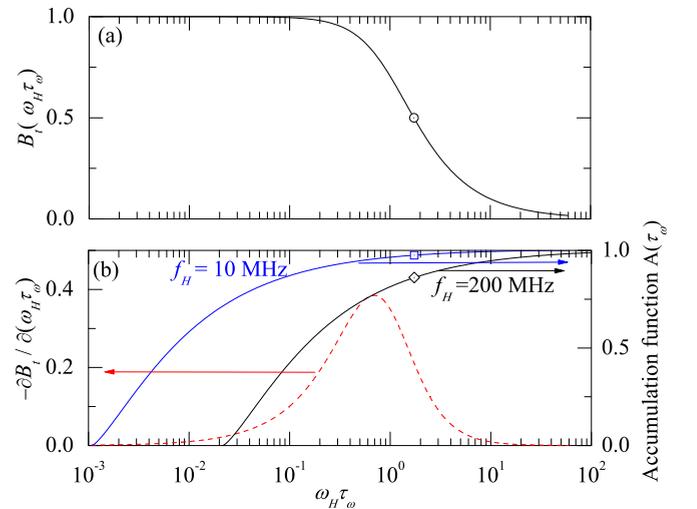
FIG. 4. (Color online) (a) The suppression function B_t from Eq. (5) and (b) the integral transform kernel $\partial B_t / \partial(\omega_H \tau_\omega)$, as functions of dimensionless heater frequency. These curves depend only on the product $\omega_H \tau_\omega$ and are general to all materials. (b) Also shows the MFT accumulation function A calculated for natural Si at 300 K at two particular heater frequencies. Since A is a function only of τ_ω, in this plot ω_H simply shifts the curve. The circle, square, and diamond indicate the values at $\omega_H \tau_\omega = 1.73$, chosen so that $B_t = \frac{1}{2}$ to facilitate a simplified cutoff algorithm to recover the MFT accumulation (see Sec. II D).

TABLE I. Comparison of integral transform results for the small timescale effect (present work) and the small lengthscale effect (Refs. [15] and [26]). Analogous results also exist in terms of the accumulation functions [Eq. (14)]. Consistent with Ref. [15], Λ_{bulk} is the bulk MFP, L_c is the characteristic size, and Λ_{eff} is the effective MFP. τ_ω is analogous to Λ_{bulk}, since both represent the intrinsic scattering in an infinite sample at steady state for a phonon of frequency ω.

	Timescale effect (infinite sample size)	Lengthscale effect (steady state)
Essential characteristic of subcontinuum forcing	High heating frequency: ω_H	Small characteristic size: L_c
Input function (property of bulk material)	$\text{K}_\tau(\tau_\omega)$ Thermal conductivity per MFT [W/m-s-K]	$\text{K}_\Lambda(\Lambda_{\text{bulk}})$ Thermal conductivity per MFP [W/m²-K]
Kernel function (captures subcontinuum phenomena)	$B_t(\omega_H \tau_\omega) = \frac{\tau_{\text{eff},\omega}}{\tau_\omega}$ Characteristic time effect	$B_t\left(\frac{\Lambda_{\text{bulk}}}{L_c}\right) = \frac{\Lambda_{\text{eff}}}{\Lambda_{\text{bulk}}}$ Characteristic size effect
Apparent thermal conductivity (integral transform)	$k_{\text{app}}(\omega_H) = \int_0^\infty \text{K}_\tau(\tau_\omega) B_t(\omega_H \tau_\omega) d\tau_\omega$	$k_{\text{app}}(L_c) = \int_0^\infty \text{K}_\Lambda(\Lambda_{\text{bulk}}) B_t\left(\frac{\Lambda_{\text{bulk}}}{L_c}\right) d\Lambda_{\text{bulk}}$

Importantly, this B_t function depends only on $\omega_H \tau_{\text{gray}}$ and not on any other material properties. As will be seen below in Sec. II D, B_t also serves as a kernel in an important integral transform that relates continuum (short MFT) and subcontinuum (long MFT) behaviors. Clearly the key physics separating the two regimes of B_t is the timescale of the heating period as compared to the MFT. Interestingly, a closely analogous kernel (also known as a suppression function [25–27,29]) was previously identified for a related integral transform in steady-state problems [15,26], where the physics separating continuum and subcontinuum regimes is the lengthscale of a small heater as compared to the bulk MFP. This analogy is further detailed in Table I.

All of the discussion above is based on the gray MFT model. However, in real materials the phonon MFTs (or MFPs) have a broad distribution, typically spanning two to three orders of magnitude [1,10,15,16,18], necessitating a nongray model. Beginning from kinetic theory, in close analogy to Refs. [1] and [15], we make a simple change of variables to write

$$k_{\text{bulk}} = \int_0^\infty \text{K}_\tau(\tau_\omega) d\tau_\omega. \tag{6}$$

Here $\text{K}_\tau(\tau_\omega)$ is the thermal conductivity per MFT,

$$\text{K}_\tau(\tau_\omega) = -\frac{1}{3} C_\omega v_\omega^2 \tau_\omega \left(\frac{d\tau_\omega}{d\omega}\right)^{-1}, \tag{7}$$

where the negative sign arises from swapping the limits of integration from ω to τ_ω, C_ω is the specific heat per phonon frequency, and polarization is lumped into C_ω.

Next, to construct an apparent thermal conductivity for this nongray model, the phonon population is broken into numerous bands $\Delta\tau_\omega$, each of which is approximated as gray using Eq. (4). Summing up all the band-wise contributions [33] yields the apparent thermal conductivity

$$k_{\text{app}}(\omega_H) = \int_0^\infty \left[-\frac{1}{3} C_\omega v_\omega^2 \tau_\omega \left(\frac{d\tau_\omega}{d\omega}\right)^{-1} \right] \frac{\tau_{\text{eff},\omega}}{\tau_\omega} d\tau_\omega, \tag{8}$$

which can also be written directly from kinetic theory [15]. Here $\tau_{\text{eff},\omega}$ is the effective MFT of the phonon mode of vibrational frequency ω. For low heating frequencies $\omega_H \ll \omega$, the continuum limit is recovered and $\tau_{\text{eff},\omega}(\omega) = \tau_\omega(\omega)$, while

this equality breaks down severely for $\omega_H \gg \omega$. Comparing Eqs. (8) and (4) reveals the convenient identity $B_t(\omega_H \tau_\omega) = \frac{\tau_{\text{eff},\omega}}{\tau_\omega}$, and finally the apparent thermal conductivity of the nongray model simplifies to

$$k_{\text{app}}(\omega_H) = \int_0^\infty \text{K}_\tau(\tau_\omega) B_t(\omega_H \tau_\omega) d\tau_\omega. \tag{9}$$

Equation (9) is one of the major results of this work. It is a Fredholm integral equation of the first kind and is closely related to an analogous result for the steady-state size effect in a nanostructure [e.g., Eq. (10) of Ref. [15] and Eq. (2) of Ref. [26]]. Here the short timescale effect of periodic heating reduces $\tau_{\text{eff},\omega}$ and thus k_{app}, just as the small lengthscale effect of nanostructure boundary scattering [15] reduces Λ_{eff} and k_{app}, an analogy further detailed in Table I. Thus, the physical meaning of B_t is to describe the strength of the periodic heating effect in reducing k_{app}, as shown in Fig. 4(a). More detailed discussion of the B_t function is in Sec. II D.

C. Experimental determination of $k_{\text{app}}(\omega_H)$ from phase lag

Experimentally, $k_{\text{app}}(\omega_H)$ is usually studied by analyzing the phase [40], and occasionally amplitude [41], of the surface temperature response to periodic surface heating. In this work we consider the phase. A detailed example is presented below in Sec. III C using a virtual experiment that is calculated as follows. Extending the gray BTE result of Appendix B [Eq. (B5)] to include nongray phenomena, the total heat flux at the surface is

$$q''_{\text{net}}(x = 0, t) = \int_0^\infty \frac{1}{2} v_{1D} C_\omega \Delta T [1 - d \exp(i\phi)]$$
$$\times \exp(i\omega_H t) d\omega. \tag{10}$$

Similarly, for the equilibrium temperature at the surface, the nongray extension of Eq. (B1) is

$$T_{\text{eq}}(x = 0, t) - T_\infty$$
$$= \frac{\int_0^\infty \frac{1}{2} v_{1D} C_\omega \Delta T [1 + d \exp(i\phi)] \exp(i\omega_H t) d\omega}{\int_0^\infty v_{1D} C_\omega d\omega}. \tag{11}$$

Thus, the surface phase lag ψ of the equilibrium temperature with respect to the heat flux at the surface is obtained

from

$$\frac{q''_{\text{net}}(x=0,t)}{T_{\text{eq}}(x=0,t) - T_\infty} = R \exp[i\psi], \qquad (12)$$

where both R and ψ are real numbers.

The physical origin of the phase lag in Eq. (12) is purely due to subcontinuum effects, whereas the phase lags reported in FDTR literature [18,40] involve both subcontinuum and continuum effects. Those FDTR measurements use a small (~microns) spot size, and, as the angular heating frequency ω_H increases, the thermal penetration depth decreases, causing the classical heat diffusion problem to transition from a spherical point source regime to a plane source regime. The corresponding phase lag thus increases from 0° (spherical source) to 45° (plane source) due to purely Fourier-law effects. In addition, at large ω_H, nondiffusive effects also become important, causing the phase to roll off even more quickly, the effects of which have been analyzed using modified Fourier-law models [18,40]. In contrast, the present work considers a planar heat source, removing a lengthscale from the problem and ensuring that the continuum Fourier-law solution exhibits a constant phase of 45° for all frequencies. Any deviations from 45° correspond unambiguously to nondiffusive effects [Eq. (12)], which we analyze using a BTE rather than Fourier treatment.

Taking the phonon dispersion relation [and thus $C_\omega(\omega)$ and $v_\omega(\omega)$] as known, Eqs. (10) to (12) show how to calculate ψ from $\omega_H \tau_\omega$. In an experiment it is natural to attempt the inverse problem: Given a set of measured ψ, what is the best estimate of τ_ω distribution? This is challenging but possible for a single Fredholm integral equation [26,42]. However, inversion of Eq. (12) to estimate τ_ω is much more complicated because it involves the ratio of two integrals. Thus, instead of solving the general inverse problem, as shown in Fig. 1, here we use the forward solution to fit a simple τ_ω function with a small number of adjustable parameters. For example, assuming a scattering law such as $\tau_\omega^{-1} = D\omega^n$, fitting experimental ψ yields D and n. Finally, intermediate quantities such as $K_\tau(\tau_\omega)$ and $k_{\text{app}}(\omega_H)$ are then calculated from Eqs. (7) and (9), as shown in more detail in Sec. III C. A key difference compared to previous work [2,16] is that here the subcontinuum effects seen in the measurements are analyzed self-consistently using a subcontinuum BTE solution rather than a modified continuum Fourier's law.

D. k accumulation with respect to MFT

We now consider the different approaches to quantifying the broad distribution of scattering strengths experienced by phonons. Previously this has been described with an accumulation function with respect to MFP, using a characteristic size to provide confinement to MFP, such as heating laser spot size [16] or Fourier-law penetration depth [2,18]. However, for the periodic heating problem here we find the analysis to be more natural and rigorous for accumulation with respect to MFT rather than MFP. Fundamentally this is because the key quantities in the BTE solution depend most directly on $\omega_H \tau_\omega$. In particular, for the planar source problem, non-Fourier behavior is clearly due to the $B_t(\omega_H \tau_\omega)$ suppression function given in Eq. (5). This is physically expected because the

forcing that drives subcontinuum behavior is fundamentally a timescale, the heater frequency ω_H, and thus should be compared to another timescale representing the phonon scattering, for which the most natural choice is τ_ω.

It is also possible to recast B_t in terms of lengthscales. A previous paper [2] implicitly did this by converting ω_H to a Fourier-law penetration depth using $L_p = \sqrt{2k/C\omega_H}$, where k is the bulk thermal conductivity and C is the total volumetric specific heat, and converting $\Lambda_{\text{bulk}} = v_{1D}\tau_\omega$, so that $\omega_H \tau_\omega \rightarrow \frac{2k\Lambda_{\text{bulk}}}{Cv_{1D}L_p^2}$. This last form may be considered less physically satisfying for several reasons: It involves a greater number of material parameters, including some from the dispersion relation; it invokes Fourier-law concepts for a strongly non-Fourier regime; and there is ambiguity about whether the k and C used should represent the full phonon population or only a subset thereof (e.g., acoustic or acoustic + optical modes). In contrast, expressing the dimensionless function B_t directly as a function of $\omega_H \tau_\omega$ makes it a universal function general to any material. The B_t function depends only on the combination $\omega_H \tau_\omega$ and is independent of the dispersion relation and the specific scattering laws (D,n) separately. Thus, for the heating-frequency-dependent measurement, we conclude that the accumulation function with respect to MFT is more suitable to capture the physics of the distribution of phonon scattering. A more detailed comparison between MFT- and MFP-based analyses is given in Sec. III C.

Similar to thermal conductivity accumulation with respect to MFP [1,10,15,16], $A(\Lambda_{\text{bulk}})$, we introduce the accumulation function with respect to MFT as

$$A(\tau_A) = \frac{1}{k_{\text{Fourier}}} \int_0^{\tau_A} K_\tau(\tau_\omega) d\tau_\omega, \qquad (13)$$

where $A(\tau_A)$ represents the fraction of the total thermal conductivity contributed by phonons with MFTs less than τ_A and k_{Fourier} is the bulk thermal conductivity. After some manipulations and integrating by parts [15], the apparent thermal conductivity in Eq. (9) can be expressed as

$$\frac{k_{\text{app}}(\omega_H)}{k_{\text{Fourier}}} = -\int_0^\infty A(\tau_\omega) \frac{dB_t}{d(\omega_H \tau_\omega)} d(\omega_H \tau_\omega). \qquad (14)$$

Like Eq. (9), this integral equation shows how to convert between the bulk MFT spectrum represented by $A(\tau_\omega)$ and the apparent frequency-dependent thermal conductivity $k_{\text{app}}(\omega_H)$, via the kernel B_t, and has an analogous counterpart for length-scale effects in steady state problems [15,26]. This integral equation separates the bulk material properties, contained in $A(\tau_\omega)$, from the effect of periodic forcing, contained in the universal function $\frac{dB_t}{d(\omega_H \tau_\omega)}$ (or B_t function).

Equations (9) and (14) also permit a graphical explanation of why the apparent thermal conductivity depends on heating frequency ω_H. For example, from Eq. (14) we see that $-\frac{dB_t}{d(\omega_H \tau_\omega)}$ acts as a sampling window [red dashed curve in Fig. 4(b)], which multiplies $A(\tau_\omega)$, with the area under the product proportional to k_{app}. Since $A(\tau_\omega)$ is strictly a function of τ_ω, plotting $A(\tau_\omega)$ on an $\omega_H \tau_\omega$ axis requires specifying the heating frequency, with larger ω_H shifting the curve to the right [compare blue and black curves in Fig. 4(b)]. Thus, as ω_H increases, there is less area under the product of the red

and black curves than under the product of the red and blue curves corresponding to lower k_{app} at higher ω_H.

Solving the inverse problem to estimate accumulation functions from the measured apparent thermal conductivity has also attracted much attention recently [2,18,26,29,42]. To obtain a simple analytical expression that still captures the main physics, we develop an approximation method here. Referring to Fig. 4(a), we approximate B_t as a Heaviside step function,

$$B_t(\omega_H \tau_\omega) \approx H(1.73 - \omega_H \tau_\omega) \approx H(0.28 - f_H \tau_\omega). \quad (15)$$

We elect to place the step edge at $\omega_H \tau_\omega = 1.73$, found numerically, because that is where $B_t = \frac{1}{2}$, as indicated by the circle in Fig. 4(a). Equation (15) makes the sampling window $-\frac{dB_t}{d(\omega_H \tau_\omega)}$ a Dirac δ function, and thus from Eq. (14)

$$\frac{k_{app}(t_c)}{k_{Fourier}} \approx A(\tau_\omega = t_c), \quad (16)$$

where $t_c \approx \frac{1.73}{\omega_H} \approx \frac{0.28}{f_H}$ is a characteristic time. This means with $k_{app}(\omega_H)$, we can directly recover $A(\tau_\omega)$, the accumulation function with respect to MFT, without inverse integral transforms, numerical manipulation, or knowledge of the dispersion relation. This approximation will be shown to give reasonable results for model calculations of pure materials and alloys, as detailed in Sec. III B.

A physical interpretation of Eq. (15) is that phonons with $\tau > t_c$ contribute nothing to heat conduction, while phonons with $\tau < t_c$ contribute fully. Thus Eq. (15) is a cutoff approximation, similar in spirit to Koh and Cahill's [2] postulate comparing the bulk phonon MFP to the Fourier-law penetration depth. However as noted above, for systems where the subcontinuum forcing is periodic heating, it is more physical to define any cutoff condition in terms of the timescales rather than lengthscales.

E. Numerical lattice BTE for verification of gray model

To verify the analytical BTE solutions of our gray model, we use a numerical method, the lattice BTE (LBTE) [32]. A detailed explanation can be found in Ref. [32]. The essence of this method is to constrain the phonons by lattice site. The time step Δt and space step Δx are related by $\Delta x = v_{1D} \Delta t$. We use $\Delta x = 0.025 \Lambda_{gray}$ and represent the semi-infinite domain with a large but finite thickness $20\Lambda_{gray}$. This is sufficient because at even the lowest ω_H of interest (e.g., $\omega_H \tau_{gray} = 10^{-2}$, which approaches the diffusive limit), $20\Lambda_{gray}$ is still at least double the penetration depth. The chosen simulation time is $\frac{10\pi}{\omega_H}$, which has been verified as long enough to reach the steady-periodic solution independent of the initial condition.

III. CASE STUDY: Si AND SiGe

Silicon has been chosen as the main example. For the gray LBTE, to make a direct comparison with Regner et al. [18] we use the same parameters: a gray MFP of 41 nm, specific heat of 1.66×10^6 J/m^3-K, and 3D sound velocity of $v_{Sound} = 6733$ m/s. For the nongray model, we use the same BvK dispersion and scattering parameters as our previous work [15].

A. Gray model

1. Equilibrium temperature and penetration depth

Detailed derivations for the gray model are given in Appendices A and B. The equilibrium temperature amplitude is $\| \frac{T_{eq}(x) - T_\infty}{\Delta T} \| = \frac{1}{2} \sqrt{1 + d^2 + 2d \cos \phi} \exp(-x \frac{b}{v_{1D} \tau_{gray}})$, from Eq. (B2), with $v_{1D} = \frac{1}{\sqrt{3}} v_\omega$, as discussed in Appendix C. This spatial profile is compared to the Fourier limit in Fig. 5. When the phonons have sufficient time to reach local equilibrium ($\omega_H \tau_{gray} \ll 1$), the analytical solution approaches the Fourier limit, with increasing deviations for larger $\omega_H \tau_{gray}$. For instance, at the surface $x = 0$, the difference between BTE and Fourier solutions for the amplitude of equilibrium temperature oscillation $\|T_{eq}(x = 0) - T_\infty\|$ increases from 0.7% at $\omega_H \tau_{gray} = 10^{-4}$ to 6.8% at $\omega_H \tau_{gray} = 10^{-2}$. As seen in Fig. 6(a), for even larger $\omega_H \tau_{gray}$ this BTE surface temperature amplitude approaches half of the Fourier limit. This surface temperature slip indicates the nondiffusive effect because the amplitude of the backward flow $T^-(x = 0) - T_\infty$ at the surface is much smaller than that of the forward flow $T^+(x = 0) - T_\infty$, which is taken as a boundary condition: See Appendix B.1 in the high frequency regime. Thus, after averaging, the equilibrium amplitude $T_{eq}(x = 0) - T_\infty$ at high ω_H is only half of the forward amplitude.

The BTE result for the penetration depth at which temperature amplitude decays to e^{-1} of its surface value is

$$L_p = \frac{v_{1D} \tau_{gray}}{b}. \quad (17)$$

Compared to the familiar Fourier-law penetration depth $L_{p,F}$, this is $L_p = L_{p,F} \frac{\sqrt{\frac{1}{2}\omega_H \tau_{gray}}}{b}$. This L_p is identical to the results obtained by Regner et al. [29] using a Milne-Eddington approximation. Figure 6(b) shows that L_p correctly
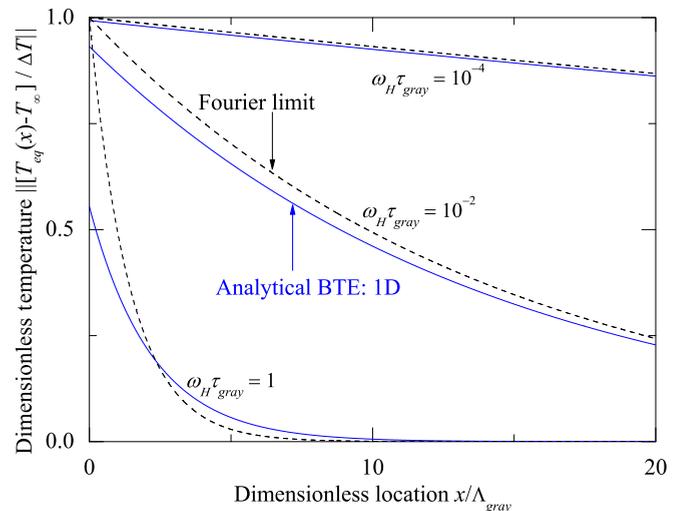
FIG. 5. (Color online) Spatial distribution of the amplitude of normalized equilibrium temperature for three different heating frequencies. The analytical BTE solution of Eq. (B2) (blue solid line) is compared with the classical Fourier limit (Ref. [43]) (black dashed line). Because our boundary condition uses ΔT as the amplitude of only the T^+ oscillation, the resulting solution for T_{eq} exhibits slip at higher frequencies.
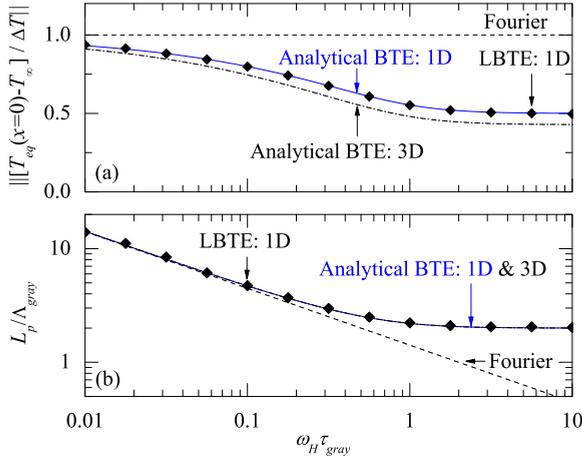
FIG. 6. (Color online) Heating-frequency dependence of (a) the surface temperature amplitude $||[T_{eq}(x = 0) - T_\infty]/\Delta T||$ and (b) penetration depth L_p for the gray model. The analytical BTE solutions (blue solid lines) for surface temperature from Eq. (B2) and penetration depth from Eq. (B4) are verified by numerical LBTE solutions (black diamonds). The BTE solutions considering 3D velocity are included for comparison (black dot dashed lines). The Fourier limits (dashed) are also shown for comparison at low heating frequency.

approaches the Fourier limit for $\omega_H \tau_{\mathrm{gray}} < 0.1$, while approaching a constant for $\omega_H \tau_{\mathrm{gray}} > 2$. These BTE solutions have been verified by the LBTE calculations across all frequency regimes, as shown in Fig. 6 by the black diamonds.

The penetration depth in the 3D BTE solution has the same form as Eq. (17) except v_{1D} is replaced with $v_{3D} = \beta v_\omega$, where the coefficient β depends on the choice of 3D solution scheme (Appendix D; $\beta = 2/3$ in our method). Thus, the surface temperature amplitude is $\|\frac{T_{eq}(x=0)-T_\infty}{\Delta T}\| = \frac{1}{2}\sqrt{1 + d_{3D}^2 + 2d_{3D}\cos\phi_{3D}}$. In this 3D case, due to the phonon's angular distribution only part of their energy is directed along the x direction, making the temperature amplitude smaller than the 1D case, as shown in Fig. 6(a). The 3D penetration depth is $\frac{v_{3D}\tau_{\mathrm{gray}}}{b}$, differing from the 1D L_p by only a coefficient. Thus, after normalizing the 1D penetration depth to $\Lambda_{\mathrm{gray},1D} = v_{1D}\tau_{\mathrm{gray}}$ and the 3D penetration depth to $\Lambda_{\mathrm{gray},3D} = v_{3D}\tau_{\mathrm{gray}}$, the functions become identical, as shown in Fig. 6(b).

2. Surface heat flux and phase lag

The surface heat flux for the gray BTE model is shown in Fig. 7(a), normalized to the Fourier limit $q''_{\mathrm{Fourier}} = k_{\mathrm{Fourier}}\Delta T\sqrt{\frac{\omega_H}{\alpha}}$, where α is the thermal diffusivity and verified by LBTE simulations. The BTE solution clearly converges to the Fourier result for small heater frequencies. In the opposite limit we find $\frac{q''_{\mathrm{BTE}}}{q''_{\mathrm{Fourier}}} = \frac{1}{2\sqrt{\omega_H \tau_{\mathrm{gray}}}}$ from Eq. (B6), which means Fourier's law overpredicts the heat flux caused by a prescribed surface temperature oscillation. This is equivalent to the BTE solution exhibiting a reduction in apparent thermal conductivity. From Eq. (B5) the heat flux amplitude in this large $\omega_H \tau_{\mathrm{gray}}$ limit is $q''_{\mathrm{BTE}} = \frac{1}{2}v_{1D}C\Delta T$. It is independent of τ_{gray}, which means nondiffusive transport. As with the surface
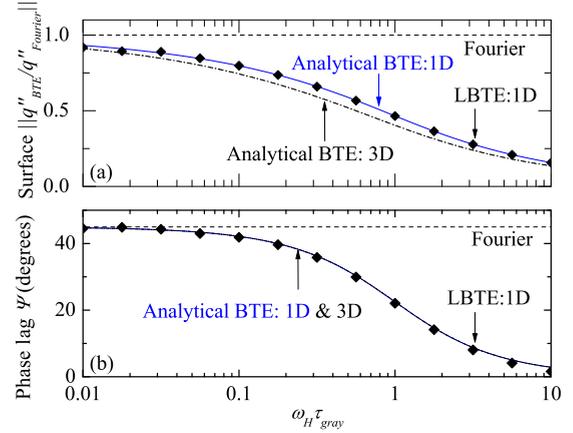
FIG. 7. (Color online) Heating-frequency dependence of the gray BTE results for (a) the amplitude of surface heat flux and (b) phase lag of the surface temperature compared to surface heat flux. The analytical BTE solution of surface heat flux from Eq. (B6) and phase lag from Eq. (B8) (blue solid lines) are verified by a numerical LBTE solution (black diamonds). The BTE solutions considering 3D velocity effects are also shown (black dot dashed lines). The Fourier limits (dashed lines) are recovered at low heating frequency.

temperature, in the 3D case the heat flux is also smaller than the 1D case.

The phase lag of the surface equilibrium temperature as compared to surface heat flux is $\psi_{\mathrm{gray}} = \tan^{-1}(-\frac{2d\sin\phi}{1-d^2})$, which is shown in Fig. 7(b). For small $\omega_H\tau_{\mathrm{gray}}$ the BTE solution of Eq. (B8) correctly approaches the well-known Fourier limit for planar periodic heating, $\psi = 45°$. In the large $\omega_H\tau_{\mathrm{gray}}$ limit, the heat transport gradually becomes nondiffusive, and the phase lag decreases to zero. In the 3D case, the phase lags exactly match those of the 1D BTE solution because ψ_{gray} for both is independent of the group velocity and thus β.

3. Apparent thermal conductivity of gray model: Dependence on heater frequency or penetration depth

The ω_H-dependent apparent thermal conductivity, which is defined in Eq. (4) for the gray model, is shown in Fig. 8(a). As $\omega_H\tau_\omega$ increases, $k_{\mathrm{BTE}}/k_{\mathrm{Fourier}}$ decreases monotonically to zero, with the same results for both 1D and 3D gray models. Because of the emphasis on MFPs in this field, it is common to transform ω_H to a corresponding Fourier-law penetration depth using $L_{p,KC} = \sqrt{\frac{2\alpha_{\mathrm{low}}}{\omega_H}}$, where the subscript KC denotes the Koh and Cahill treatment [2] and α_{low} is the thermal diffusivity in the limit of low heating frequency, e.g., the classical handbook value. In Koh and Cahill's approach [2], $L_{p,KC}$ acts as a cutoff threshold such that phonons with bulk MFPs longer than $L_{p,KC}$ do not contribute at all to heat conduction. Regner et al. [18] used a very similar cutoff conduction except that the critical penetration depth was defined using the apparent thermal diffusivity, namely, $L_{p,\mathrm{Regner}} = \sqrt{\frac{2\alpha(\omega_H)}{\omega_H}}$, where now $\alpha(\omega_H)$ itself depends on heater frequency through $k_{\mathrm{app}}(\omega_H)$. In the low-frequency limit, $L_{p,\mathrm{Regner}} = L_{p,KC} = L_p$, where the latter is the e^{-1} penetration depth for the BTE solution given in Eq. (B4), while at high frequency $L_{p,\mathrm{Regner}} < L_{p,KC} < L_p$. To facilitate comparisons with the LBTE results of Regner et al. [18], Fig. 8(b) plots our results in terms of $L_{p,\mathrm{Regner}}$. The
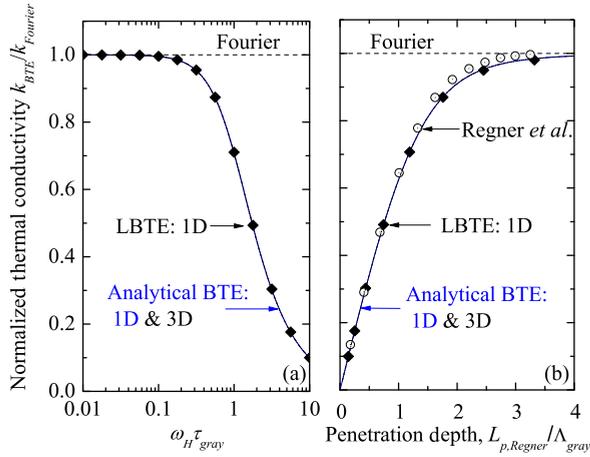
FIG. 8. (Color online) (a) Normalized apparent thermal conductivity of Si at 300 K for the gray model as functions of (a) heating frequency and (b) Fourier-law penetration depth. The analytical BTE solutions of Eq. (4) (solid lines) and numerical LBTE results (black diamonds) are in excellent agreement with each other, and both recover the classical Fourier limit (dashed lines) where appropriate. The results from an LBTE simulation by Regner *et al.* (Ref. [18]) are also shown for comparison (open circles).

comparison shows excellent agreement between our analytical and LBTE solutions over the entire L_p range. Furthermore, it is reassuring that these results for k_{BTE} also exhibit very good agreement with the LBTE results of Regner *et al.* [18] even though the two approaches began with different surface forcing conditions (prescribed T^+ in our case; prescribed q in Ref. [18]). The two LBTE solution in Fig. 8(b) do exhibit some minor disagreement ($\sim 2.7\%$) in the transition regime, although the reasons for this are not known.

B. Nongray model: Heating-frequency-dependent thermal conductivity

To account for the typically broad distribution of phonon FMP [1,10,15,16,18], we incorporated the phonon MFP distribution for two model materials into Eq. (8) and obtained the nongray $k_{\mathrm{app}}(\omega_H)$, as shown in Fig. 9, based on the analytical gray solution of Sec. II B. The nongray model captures the characteristic of the long MFT tail [see Fig. 10(c)], which results in a stronger heating-frequency dependence than in the gray model ($\tau_{\mathrm{gray}} = 6.0\,\mathrm{ps}$). Although the natural Si measurements by Koh and Cahill [2] and Wilson and Cahill [24] did not exhibit any clear ω_H effect, those experiments were limited to $f_{H,\max} = \omega_{H,\max}/2\pi = 10\,\mathrm{MHz}$–17.6 MHz, respectively, which according to the calculations of Fig. (9) corresponds to a reduction by less than 3%, which likely is difficult to observe above experimental noise.

However, strongly ω_H-dependent k_{app} for several semiconductor alloys, namely $\mathrm{Si}_{1-x}\mathrm{Ge}_x$, $\mathrm{In}_{1-x}\mathrm{Ga}_x\mathrm{P}$, and $\mathrm{In}_{1-x}\mathrm{Ga}_x\mathrm{As}$, has been observed [2,24]. We use the undoped $6\,\mu\mathrm{m}$ thick $\mathrm{Si}_{0.4}\mathrm{Ge}_{0.6}$ film of Ref. [2] for comparison with our present nongray model. We normalize those measurements using a bulk reference value for undoped $\mathrm{Si}_{0.4}\mathrm{Ge}_{0.6}$ of $k_{\mathrm{Fourier}} \approx 8.3\,\mathrm{W/m\text{-}K}$ [44]. To model the $\mathrm{Si}_{0.4}\mathrm{Ge}_{0.6}$, we use the virtual crystal approximation [45] and a BvK dispersion [15] based
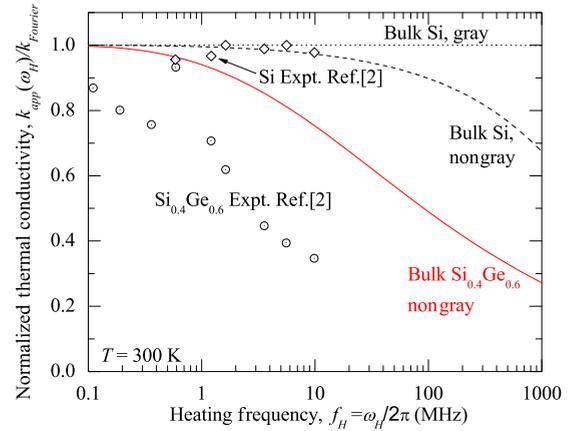
FIG. 9. (Color online) Heating-frequency dependence of apparent thermal conductivity for Si (black dashed line) and $\mathrm{Si}_{0.4}\mathrm{Ge}_{0.6}$ (red solid line) for the nongray BTE model described in the text. The measurements (Ref. [2]) (points) of $\mathrm{Si}_{0.4}\mathrm{Ge}_{0.6}$ and Si are also included for comparison.

on a primitive unit cell density of $2.3 \times 10^{28}\,\mathrm{m}^{-3}$ and averaged sound velocity of 4630 m/s. The main scattering mechanism in $\mathrm{Si}_{0.4}\mathrm{Ge}_{0.6}$ is alloy scattering. The alloy scattering coefficient $A_{\mathrm{alloy}} = 6.7 \times 10^{-42}\,\mathrm{s}^3$, obtained by fitting the reference value of k_{Fourier} [44], is more than three orders of magnitude larger than A_{isotope} for natural Si [15]. The resulting $k_{\mathrm{app}}(\omega_H)$ for the alloy is calculated from Eq. (9) and shown in Fig. 9 (red line). Comparing the nongray calculations for Si and $\mathrm{Si}_{0.4}\mathrm{Ge}_{0.6}$ reveals the important observation that the k_{app} suppression occurs at much lower frequencies in the alloy than in the pure single crystal. For example, at $f_H = \omega_H/2\pi = 10\,\mathrm{MHz}$, the reduction is only 2.7% for Si but 25% for $\mathrm{Si}_{0.4}\mathrm{Ge}_{0.6}$. This indicates that phonons with large MFTs play a more important role in the thermal conductivity of the alloy than in the pure crystal, consistent with earlier calculations of the MFP distributions of these materials [1,46,11]. We also note that an FDTR measurement of crystalline Si up to 100 MHz showed stronger frequency dependence [18]. For consistency in comparing results for Si and $\mathrm{Si}_{1-x}\mathrm{Ge}_x$ alloy, in Fig. 9 we elect to only show the results that were both obtained using the same TDTR technique [2].

Figure 9 also compares our $\mathrm{Si}_{0.4}\mathrm{Ge}_{0.6}$ calculation with the corresponding experimental data from Ref. [2]. The measurements have the same general trend but show an even stronger ω_H effect. There are two important distinctions between the model and experiment that could explain the stronger suppression seen in the latter. First, considering the very broad MFP distribution expected for $\mathrm{Si}_{1-x}\mathrm{Ge}_x$, [1,11], the film thickness of $6\,\mu\mathrm{m}$ may cause additional suppression, which is not captured in the present calculation for a semi-infinite substrate. Also, a size-effect reduction may arise from the finite Gaussian beam radii used in the experiment (6.5–15 $\mu\mathrm{m}$), whereas the model deals with an infinite plane source.

Although due to the different experimental geometries these calculations cannot be directly compared to Koh and Cahill's measurement [2], the modeling results still are insightful because they use the BTE to isolate an ω_H effect in reducing k_{app}. Furthermore, this reduction can be strong in semiconductor alloys even for $f_H = \omega_H/2\pi$ as small as
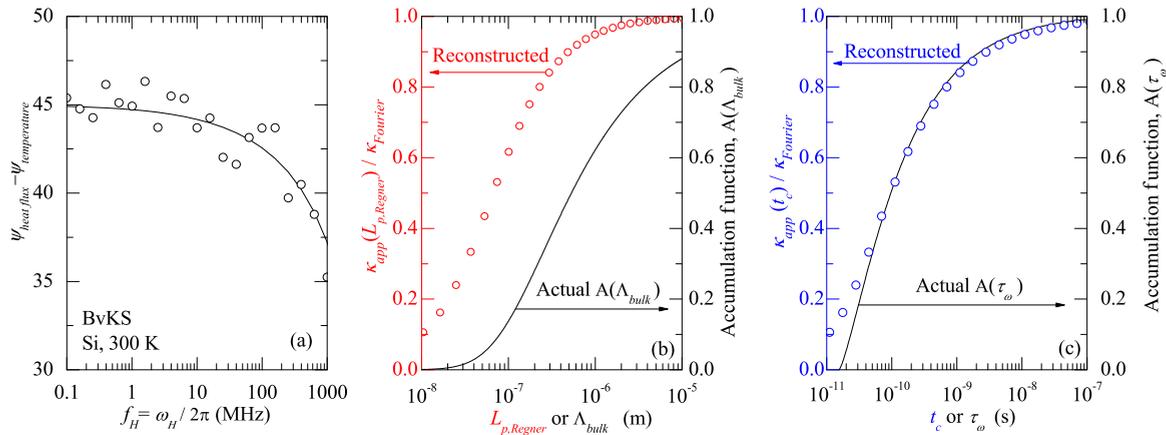
FIG. 10. (Color online) Comparison of MFP and MFT approaches to analyzing a virtual experiment. (a) Calculated ideal phase lag (black solid line) for BvKS Si, and the same with $\pm 2°$ error to represent a virtual experiment (circles) (b) Left axis: Penetration depth dependent thermal conductivity using power-law MFT fit from virtual experiment (circles). Right axis: Actual accumulation function $A(\Lambda_{\text{bulk}})$ including all scattering (solid line). (c) Left axis: Characteristic time t_c dependent thermal conductivity using power-law MFT fit from virtual experiment (circles). Right axis: Actual accumulation function $A(\tau_\omega)$ including all scattering (solid line).

$\sim$10 MHz, frequencies at least two orders of magnitude lower than what might be expected based on a typically used dominant phonon MFT of $\sim$100 ps [2]. However, the lower frequency onset is also consistent with more detailed calculations of the MFT accumulation. For instance, in the case of $Si_{0.4}Ge_{0.6}$, we find the range of important MFTs spans from $\sim$20 ps to $\sim$130 ns (10%–90% cutoffs), a range of over 6000:1. This breadth, and the shift towards timescales much larger than the dominant phonon expectation of $\sim$100 ps, is also consistent with earlier calculations of the MFP distribution of $Si_{1-x}Ge_x$ alloys by ourselves [1,46] and others [11].

C. Measuring accumulation function with respect to MFT instead of MFP: a virtual experiment

To show how the framework of Fig. 1 can be used to measure the accumulation function, we performed a virtual experiment based on the phase lag between surface temperature and surface heat flux, as shown in Fig. 10. The calculations are for Si at 300 K, using a BvK dispersion with strong umklapp ($\tau_\omega^{-1} = 1.53 \times 10^{-19} T \cdot \omega^2$, with unit of s^{-1}) and weak impurity ($A_{\text{impurity}} = 2.54 \times 10^{-45} s^3$). For completeness in fitting we also included a finite boundary scattering length ($\Lambda_{\text{bdy}} = v\tau_{\text{bdy}} = 5.7$ mm) [15], although this has a negligible impact on the room temperature calculations presented here. In Fig. 10(a), the ideal ψ response is calculated for the model (solid line), while the virtual experiment has ψ points randomized within $\pm 2°$ to represent measurement error (empty circles). Following the flowchart of Fig. 1, we fit this $\psi(\omega_H)$ data with Eq. (12) using a known single-branch BvK dispersion relation and unknown scattering power law $\tau_\omega^{-1} = D\omega^n$. This two-parameter fit yields $D = 1.43 \times 10^{-19} T \text{ s}^{-3}$ and $n = 2.00$, in very good agreement with the actual umklapp parameters used. With the fitted D and n, we calculate $k_{\text{app}}(\omega_H)$ from Eq. (9), then convert $k_{\text{app}}(\omega_H)$ from frequency domain to length domain in Fig. 10(b) and time domain in Fig. 10(c).

These results support the argument for representing accumulation, and developing cutoff approximations, with respect

to MFT rather than the much more common approach with respect to MFP. To see this, we compare the actual accumulations functions (lines) with their approximate reconstructions (circles), using both time- and length-based approaches. For the reconstructed data in Fig. 10(b) (red circles), for the x axis we convert ω_H to $L_{p,\text{Regner}}$ using $L_{p,\text{Regner}} = \sqrt{\frac{2\alpha(\omega_H)}{\omega_H}}$ and the y axis to $k_{\text{app}}/k_{\text{Fourier}}$. If the penetration depth cutoff postulate [16,18] is suitable for periodic planar heating, this plot of $k_{\text{app}}/k_{\text{Fourier}}$ versus $L_{p,\text{Regner}}$ (circles) should match the actual accumulation function $A(\Lambda_{\text{bulk}})$ (line). However, as shown in Fig. 10(b), the agreement is poor, with the two curves differing by a factor of $\sim$8 along the Λ_{bulk} axis.

The agreement is much better using the MFT approach. For the reconstructed curve of Fig. 10(c) (blue circles), we now change the x axis to characteristic time $t_c \approx \frac{1.73}{\omega_H}$ and the y axis to $k_{\text{app}}(t_c)/k_{\text{Fourier}}$. [Recall that the coefficient 1.73 gives the best step-function approximation to the actual suppression function of Fig. 4(a).] Now, if the MFT cutoff postulate is appropriate, this plot of $k_{\text{app}}/k_{\text{Fourier}}$ versus t_c should recover the actual MFT accumulation function $A(\tau_\omega)$. As shown in Fig. 10(c), the agreement is excellent over more than three orders of magnitude of MFT. An approximate justification for this MFT-based cutoff treatment was discussed in Fig. 4(a). The kernel function B_t acts as a sampling function, which heavily suppresses the contributions from phonons with MFT longer than the characteristic time t_c, crudely following the shape of a step function. Therefore, ω_H is directly related to cutoff MFT, which can be used to probe the accumulation function over MFT. Thus, the comparisons between actual and reconstructed data in Figs. 10(b) and 10(c) confirm that for this periodic planar heating system, a cutoff approach is much more appropriate in the MFT domain than MFP domain.

IV. SUMMARY AND CONCLUSIONS

An analytical solution to the BTE for the periodic plane-source heating problem has been obtained based on the gray MFT model. This model has been verified by our

LBTE simulations as well as LBTE results from the literature [18]. The BTE solution was extended to the nongray MFT regime through a frequency-integrated gray-medium treatment [27,30]. This model shows how to construct an accumulation function with respect to MFT from measured phase lag data, both directly and from an intermediate calculation of the apparent thermal conductivity. The BTE solution confirms that the fundamental reason for the frequency-dependent thermal conductivity is that phonons with MFTs longer than the characteristic heating time conduct less heat than classically expected. Therefore, for a system such as this, which is driven purely by a fast timescale, it is most natural to describe the breakdown of Fourier's law using an apparent thermal conductivity that depends on the driving timescale, rather than converting it to some equivalent lengthscale such as a classical penetration depth. The timescale description is also cleaner than the lengthscale description because the former does not introduce other material properties such as diffusivity. The model has been applied to Si and $Si_{0.4}Ge_{0.6}$, and it agrees qualitatively with the experimental reports [2,24] that heating frequencies up to 20 MHz cause a strong suppression of thermal transport in the alloy but a negligible suppression in natural Si. This model has also been applied to a virtual FDTR experiment, which fits the phase lag between surface temperature and heat flux to fix the parameters of a power-law MFT. The results show that a cutoff approach is much more accurate using timescales than equivalent converted lengthscales, with the former giving very good agreement with the actual MFT accumulation function used for over four orders of magnitude of τ_ω.

APPENDIX A: BTE SOLUTIONS IN FORWARD AND BACKWARD DIRECTIONS

This appendix describes the solution of the BTE [Eq. (1)]. Rather than directly solving for the distribution function, we make the radiation analogy and use phonon intensity [39]. The phonon intensity per unit time, per unit area, per phonon frequency, and per unit solid angle is

$$I_\omega = \sum_s |v_{\omega,s}| \hbar \omega D(\omega) f_\omega, \qquad (A1)$$

where s represents the polarizations and $D(\omega)$ is the density of states of the sth branch. For simplicity we lump the three acoustic branches into one, as discussed in Sec. II A. Thus, in the 1D case of Fig. 3(a), the BTE is recast as

$$\frac{\partial I_\omega}{\partial t} + v_{1D} \frac{\partial I_\omega}{\partial x} = \frac{I_\omega^0 - I_\omega}{\tau_\omega}, \qquad (A2)$$

where $v_{1D} = \frac{v_\omega}{\sqrt{3}}$ is the effective group velocity in the x direction (see Appendices C and D) and I_ω^0 is the equilibrium phonon intensity. Strictly, I_ω^0 is an average over all phonon directions and frequencies [30,47]. This is trivial for the gray MFT solution since there is only one ω to consider. However, in the general nongray case, the corresponding BTE can only be solved numerically using techniques such as Monte Carlo [47], discrete ordinates [34,48], finite volumes [49], or the LBTE method [18]. On the other hand, analytical solutions have great advantages for understanding the essential physics and reducing computational time. To facilitate such an analytical solution for the general nongray case, we assume that the true I_ω^0 integral can be approximated adequately by a simpler form whereby phonons with the same frequency reach their own equilibrium. This approach has been used previously [27,30], and the resulting "frequency-integrated gray-medium" treatment was found to yield surprisingly good agreement with numerical solutions of the full nongray BTE for Si and PbSe [27]. Combining this assumption with the governing equation in Eq. (A2) and periodic heating boundary conditions described in the next subsection, the BTE is analytically solvable.

Equation (A2) can be solved by different approximation methods such as two-flux (or Schuster-Schwarzschild) model and Milne-Eddington model [31]. Both models assume the phonon intensities are isotropic over the forward and backward hemispheres but with different amplitudes [31], respectively. Some differences between these models are discussed in Appendix D. In the usual way, we multiply Eq. (A2) by μ and integrate over forward and backward hemispheres of solid angle. Thus, the BTE in Eq. (A2) separates into two coupled equations with respect to the forward flux q^+ and backward flux q^-. For truly 1D transport as depicted in Fig. 3(a), $\mu = 1$. We will first study this case and discuss the general 3D case of Fig. 3(b) in Appendix D.

In the forward direction, Eq. (A2) of the gray model becomes

$$\frac{\partial q^+}{\partial t} + v_{1D} \frac{\partial q^+}{\partial x} = \frac{q^0 - q^+}{\tau_{\text{gray}}}. \qquad (A3)$$

The counterpart equation in the backward direction has the same form except with q^- instead of q^+. The equilibrium q^0 couples the forward and backward fluxes,

$$q^0 = \tfrac{1}{2}(q^+ + q^-). \qquad (A4)$$

The net heat flux is conveniently expressed as

$$q_{\text{net}}'' = q^+ - q^-. \qquad (A5)$$

Substituting Eq. (A4) into Eq. (A3), after algebraic manipulation a pair of equations for the forward and backward direction is obtained,

$$\tau_{\text{gray}} \frac{\partial^2 q^+}{\partial t^2} + \frac{\partial q^+}{\partial t} - \tau_{\text{gray}} v_{1D}^2 \frac{\partial^2 q^+}{\partial x^2} = 0 \qquad (A6)$$

and

$$\tau_{\text{gray}} \frac{\partial^2 q^-}{\partial t^2} + \frac{\partial q^-}{\partial t} - \tau_{\text{gray}} v_{1D}^2 \frac{\partial^2 q^-}{\partial x^2} = 0. \qquad (A7)$$

For the boundary conditions, a sinusoidal temperature is imposed in the positive direction at $x = 0$, as shown in

TABLE II. Key coefficients of the BTE solution, including simplified forms in low- and high-frequency limits. These expressions are derived using a gray MFT, but they can also be extended to a nongray solution with τ_ω, as explained in Sec. II B. Therefore the expressions in this table apply for both τ_{gray} and τ_ω.

Coefficient	Low ω_H limit	High ω_H limit
$a = \sqrt{\frac{\omega_H \tau_\omega}{2}}\sqrt{\omega_H \tau_\omega + \sqrt{(\omega_H \tau_\omega)^2 + 1}}$	$\sqrt{\frac{\omega_H \tau_\omega}{2}}\left(1 + \frac{\omega_H \tau_\omega}{2}\right) \approx \sqrt{\frac{\omega_H \tau_\omega}{2}}$	$\omega_H \tau_\omega + \frac{1}{8\omega_H \tau_\omega} \approx \omega_H \tau_\omega$
$b = \sqrt{\frac{\omega_H \tau_\omega}{2}}\sqrt{-\omega_H \tau_\omega + \sqrt{(\omega_H \tau_\omega)^2 + 1}}$	$\sqrt{\frac{\omega_H \tau_\omega}{2}}\left(1 - \frac{\omega_H \tau_\omega}{2}\right) \approx \sqrt{\frac{\omega_H \tau_\omega}{2}}$	$\frac{1}{2} - \frac{1}{16(\omega_H \tau_\omega)^2} \approx \frac{1}{2}$
$\cos\phi = \frac{b}{a}$	$1 - \omega_H \tau_\omega \approx 1$	$\frac{1}{4\omega_H \tau_\omega} \approx 0$
$\sin\phi = -2b$	$-\sqrt{2\omega_H \tau_\omega} \approx 0$	$-1 + \frac{1}{8(\omega_H \tau_\omega)^2} \approx -1$
$d = \frac{b}{a + \omega_H \tau_\omega}$	$1 - \sqrt{2\omega_H \tau_\omega} \approx 1$	$\frac{1}{4\omega_H \tau_\omega} \approx 0$

Eq. (2). Since the domain is semi-infinite, deep inside the body the distribution must return to the equilibrium intensity corresponding to the ambient temperature, namely

$$T^+(x = \infty, t) = T^-(x = \infty, t) = T_\infty. \tag{A8}$$

To transform these T boundary conditions to corresponding constraints on q^+ and q^-, we linearize the response. The temperature oscillations of the heat source are limited to $\Delta T \ll T_\infty$, which is typical in the measurements [2,16,20,40]. In this case, the temperature variation is a linear response to the heat flux variation in each direction, such as

$$dq^+ \approx \tfrac{1}{2} v_{1D} C \, dT^+ = \tfrac{1}{2} v_{1D} \, dU^+, \tag{A9}$$

where C is the volumetric specific heat and U is the volumetric energy density. The factor of $\frac{1}{2}$ arises from only integrating over the hemisphere. Using Eq. (A9), both temperature boundary conditions from Eqs. (2) and (A8) are transformed to heat flux boundary conditions.

1. Nondimensionalization and solution in the forward direction with gray MFT

For convenience we define the dimensionless time as $\gamma = \frac{t}{\tau_{\text{gray}}}$, location as $\chi = \frac{x}{v_{1D}\tau_{\text{gray}}}$, and forward energy flux as

$$Q^+(\chi, \gamma) = Q^+(x, t) = \frac{q^+(x, t) - q^+(x = \infty, t)}{q^+(x = 0, t = 0) - q^+(x = \infty, t)}, \tag{A10}$$

with a similar form for Q^- after substituting $q^+ \to q^-$, except keep the denominator $q^+(x = 0, t = 0)$ term the same. As $x \to \infty$, from Eqs. (A8) and (A9) we have $q^+(x = \infty, t) = q^-(x = \infty, t) = q_\infty$, and the governing Eq. (A6) simplifies to

$$\frac{\partial^2 Q^+}{\partial \gamma^2} + \frac{\partial Q^+}{\partial \gamma} - \frac{\partial^2 Q^+}{\partial \chi^2} = 0. \tag{A11}$$

Applying Eqs. (A9) and (A10) to Eqs. (2) and (A8), we obtain the boundary conditions

$$Q^+(\chi = 0, \gamma) = \exp(i\omega_H \tau_{\text{gray}} \gamma) \tag{A12}$$

and

$$Q^+(\chi = \infty, \gamma) = 0. \tag{A13}$$

Now the governing Eq. (A11), which is hyperbolic telegraph type, can be solved by a standard Laplace transform

method. After taking the Laplace transform of Eqs. (A11)–(A13) with respect to time, the resulting ordinary differential equation in χ is readily solved, and finally an inverse Laplace transform is used to obtain the time domain solution. During the inverse transform, the singularity problem is overcome using the Cauchy integral theorem [50]. Finally, we obtain the dimensionless temperature in the forward direction as

$$Q^+_{\text{gray}}(\chi, \gamma) = \exp(-b\chi)\exp(i\omega_H \tau_{\text{gray}}\gamma - ia\chi), \tag{A14}$$

where a and b are purely real and are given in Table II.

2. Solution in the backward direction with gray MFT

Beginning from Eq. (A7), the backward direction counterpart of Eq. (A11) is

$$\frac{\partial^2 Q^-}{\partial \gamma^2} + \frac{\partial Q^-}{\partial \gamma} - \frac{\partial^2 Q^-}{\partial \chi^2} = 0. \tag{A15}$$

However, there is only one obvious boundary condition,

$$Q^-(x = \infty, t) = 0. \tag{A16}$$

At $x = 0$, the heat flux in the negative direction is a depth-integrated response to the positive direction heat flux, which is not specified in advance (recall that for convenience our boundary condition at $x = 0$ was defined purely in terms of Q^+). Without one more boundary condition it would appear that we cannot solve Eq. (A15). However, energy conservation can provide the required constraint, as follows. Since the form of the governing equations in the forward and backward directions are exactly the same, we seek a solution of Eq. (A15) with the same form as Eq. (A14) while allowing for different amplitude and phase,

$$Q^-(x, t) = d\exp(-b\chi)\exp(i\omega_H \tau_{\text{gray}}\gamma - ia\chi + i\phi). \tag{A17}$$

Here d is the amplitude coefficient and ϕ is the phase shift, where d and ϕ are purely real and are determined by energy conservation. Since there is no heat generation in the material, it must always be true that

$$\nabla \cdot q''_{\text{net}} + \frac{\partial U}{\partial t} = 0, \tag{A18}$$

where the phonon energy density in Fig. 3(a) is

$$U = \frac{q^+ + q^-}{v_{1D}}. \tag{A19}$$

Substituting the forward and backward solutions into Eq. (A18), for the real part we obtain

$$[-(a - \omega_H \tau_{\text{gray}}) + d(a + \omega_H \tau_{\text{gray}})\cos\phi + db\sin\phi]$$
$$\times \sin(\omega_H t) + [b + d(a + \omega_H \tau_{\text{gray}})\sin\phi - db\cos\phi]$$
$$\times \cos(\omega_H t) = 0, \qquad (A20)$$

where the coefficients a, b, ϕ, and d are all only functions of $\omega_H \tau_{\text{gray}}$. Since Eq. (A20) is valid at all times, the coefficients of $\sin(\omega_H t)$ and $\cos(\omega_H t)$ must both be zero. Thus, we obtain

$$d = \frac{b}{a + \omega_H \tau_{\text{gray}}} \qquad (A21)$$

and

$$\cos\phi = \frac{b}{a}, \qquad (A22)$$

as given in Table II.

APPENDIX B: SOLUTIONS FOR TEMPERATURE AND HEAT FLUX IN GRAY MODEL

Using the positive and negative flux solutions from Appendix A, we now obtain the equilibrium temperature, penetration depth, net heat flux, phase lag on the surface, and apparent thermal conductivity.

1. Temperature and penetration depth

The equilibrium temperature is obtained by conserving the total energy density [35]. From the linear response of Eq. (A9) the equilibrium temperature is obtained from

$$U_{\text{eq}}(x,t) - U_\infty = C[T_{\text{eq}}(x,t) - T_\infty]. \qquad (B1)$$

Thus, the amplitude of the equilibrium temperature oscillation is

$$\left\| \frac{T_{\text{eq}}(x) - T_\infty}{\Delta T} \right\|$$
$$= \frac{1}{2}\sqrt{1 + d^2 + 2d\cos\phi}\, \exp\left(-x\frac{b}{v_{1D}\tau_{\text{gray}}}\right), \quad (B2)$$

where the term $\exp(i\omega_H t - ix\frac{a}{v_{1D}\tau_{\text{gray}}})$ does not appear because it has unity amplitude. To facilitate comparisons with the Fourier limit, it is convenient to recast this result in terms of the thermal diffusivity α by using $\alpha = v_{1D}^2 \tau_{\text{gray}} = \frac{1}{3}v_g^2 \tau_{\text{gray}}$, where the two forms correspond to 1D and 3D variations depicted in

Fig. 3. The result is

$$\left\| \frac{T_{\text{eq}}(x) - T_\infty}{\Delta T} \right\| = \frac{1}{2}\sqrt{1 + d^2 + 2d\cos\phi}$$
$$\times \exp\left(-x\sqrt{\frac{\omega_H}{2\alpha}}\frac{b}{\sqrt{\frac{\omega_H \tau_{\text{gray}}}{2}}}\right). \qquad (B3)$$

Equation (B3) also directly gives the thermal penetration depth, L_p,

$$L_p = \sqrt{\frac{2\alpha}{\omega_H}}\frac{\sqrt{\frac{1}{2}\omega_H \tau_{\text{gray}}}}{b} = L_{p,F}\frac{\sqrt{\frac{1}{2}\omega_H \tau_{\text{gray}}}}{b}, \qquad (B4)$$

where $L_{p,F} = \sqrt{\frac{2\alpha}{\omega_H}}$ is the Fourier limit of L_p. Various limits of the BTE solution are shown in Table III and serve as useful checks, such as verifying that the low ω_H limit recovers the classical Fourier solution.

2. Heat flux

The net heat flux is calculated by Eq. (A5). At the surface, $x = 0$, the heat flux amplitude is

$$\|q''_{\text{net}}\| = \frac{1}{2}v_{1D}C\Delta T\sqrt{1 + d^2 - 2d\cos(\phi)}. \qquad (B5)$$

Normalizing this to its Fourier limit we find

$$\left\| \frac{q''_{\text{net}}}{q''_{\text{Fourier}}} \right\| = \frac{1}{2}\sqrt{\frac{1 + d^2 - 2d\cos(\phi)}{\omega_H \tau_{\text{gray}}}}, \qquad (B6)$$

which correctly reduces to unity for small $\omega_H \tau_{\text{gray}}$, as shown in Table III.

3. Phase lag

For thermal conductivity experiments, measuring the phase lag between surface temperature and heat flux is more practical and accurate than measuring the temperature or heat flux amplitude directly because the phase lag is less sensitive to intensity instabilities [40]. To extract the phase lag, we express the ratio of heat flux to equilibrium temperature variation as a complex function with the purely real amplitude R_{gray} and phase lag Ψ_{gray},

$$\frac{q''_{\text{net}}(x,t)}{T_{\text{eq}}(x,t) - T_\infty} = R_{\text{gray}}\exp(i\psi_{\text{gray}}). \qquad (B7)$$

The time and space terms all cancel from the right-hand side. Substituting for $q''_{\text{net}}(x,t)$ and $T_{\text{eq}}(x,t)$, the phase lag is

TABLE III. Low- and high-frequency limits for various key results of the gray BTE model.

		Low $\omega_H \tau_\omega$ limit	High $\omega_H \tau_\omega$ limit
Temperature amplitude	$\left\| \frac{T_{\text{eq},\omega}(x) - T_\infty}{\Delta T} \right\|$	$\exp\left(-x\sqrt{\frac{\omega_H}{2\alpha}}\right)$	$\frac{1}{2}\exp\left(-\frac{x}{2\sqrt{\alpha\tau_\omega}}\right)$
Penetration depth	L_p	$L_{p,F} = \sqrt{\frac{2\alpha}{\omega_H}}$	$2\sqrt{\alpha\tau_\omega} = 2\Lambda_{\text{gray}}$
Surface heat flux amplitude	$\left\| \frac{q''_{\text{net}}}{q''_{\text{Fourier}}} \right\|$	1	$\frac{1}{2\sqrt{\omega_H \tau_\omega}}$
Phase lag	ψ_{gray}	$\frac{\pi}{4}$	0
Apparent thermal conductivity	$k_{\text{app,gray}}$	k_{Fourier}	$\frac{k_{\text{Fourier}}}{\omega_H \tau_\omega}$

found to be

$$\tan(\psi_{\text{gray}}) = -\frac{2d\sin\phi}{1-d^2}. \tag{B8}$$

The Fourier result is again recovered in the low $\omega_H \tau_{\text{gray}}$ limit, as shown in Table III.

APPENDIX C: RELATIONSHIP BETWEEN 3D AND 1D GROUP VELOCITY

We consider the relationship between the 1D velocity v_{1D} and the actual group velocity v_ω. The present work uses a heat source in the y-z plane. Due to the translational symmetry of the heating surface and the fact that the material's dispersion relation is taken to be isotropic, the net heat flow must propagate normal to the yz plane (i.e., along the x axis), suggesting a 1D treatment. However, the constituent phonons still travel in all 4π steradians, so some care is required in converting their actual group velocities to an equivalent 1D velocity v_{1D}. In the 3D phonon dispersion with a single polarization, all phonons of frequency ω travel with a group velocity of magnitude v_ω, but due to their angular distribution only part of their energy is directed along the x direction. Therefore, in this work, the relationship $v_{1D} = \frac{1}{\sqrt{3}}v_\omega$ is used [51,52]. In ideal gases, this gives the relationship between the thermal velocity and sound velocity [51]. In solids and liquids at low temperature the phenomenon is known as second sound [53,54], where it has been studied by models [55–57] and experiments in helium [58], NaF [59,60], NaI [60], SiTiO$_3$ (Ref. [61]), etc. More fundamentally, this $\frac{1}{\sqrt{3}}$ factor can also be understood as a consequence of collisions randomizing the directions of the velocity vectors [51], resulting in the effective 1D velocity v_{1D} for energy propagation.

This velocity relation can also be verified by comparing the equilibrium temperature in Eq. (B2) (or surface heat flux) at low heating frequency ω_H with the Fourier limit. The Fourier limit of temperature amplitude is $\left\| \frac{T_{\text{eq}}(x,t)-T_\infty}{\Delta T} \right\| = \exp(-x\sqrt{\frac{\omega_H}{2\alpha}})$. Comparing with our 1D model in Eq. (B2), we can obtain their relation that $v_{1D} = \sqrt{\frac{\alpha}{\tau_{\text{gray}}}} = \frac{1}{\sqrt{3}}v_\omega$.

APPENDIX D: RELATIONSHIP BETWEEN 3D AND 1D BTE MODELS

This appendix extends the BTE solution from 1D velocity v_{1D} in Fig. 3(a) to the more general case in Fig. 3(b). We also explain the similarities and subtle distinction between our two-flux treatment and the more common Schuster-Schwarzschild and Milne-Eddington approximations.

As done in Appendix A for the strictly 1D solution, for 3D we can also obtain the governing equation for phonon intensity,

$$\frac{\partial I_\omega}{\partial t} + v_\omega \mu \frac{\partial I_\omega}{\partial x} = \frac{I_\omega^0 - I_\omega}{\tau_\omega}. \tag{D1}$$

The key difference and challenge when solving Eq. (D1) is in dealing with the angle dependence of the x-direction velocity, as expressed by $v_\omega \mu$. This is commonly treated by multiplying the equation by various moments of μ and integrating over solid angle. We also use the common two-flux

approximation that the radiative intensity is hemispherically isotropic with different values in the forward and backward directions [31]. With this assumption, the governing Eq. (D1) can be simplified. For the mth moment in general, Eq. (A1) is multiplied by μ^m and integrated over the forward and backward hemispheres. In the forward direction, the mth moment $q_{\omega,m}^+$ is

$$q_{\omega,m}^+ = 2\pi \int_0^1 I_\omega^+ \mu^m d\mu. \tag{D2}$$

The 2π arises from integrating over azimuthal angle. For $m = 0$ and separating the forward and backward directions, the two-flux treatment becomes the Schuster-Schwarzschild approximation [31]. If both $m = 0$ and $m = 1$ moments are used and the integration ranges over 4π steradians, it is the Milne-Eddington approximation [29,31]. Since we are more interested in the heat flux, it is convenient to separate the forward and backward fluxes and use the first moment $q_{\omega,1}^+$ because it directly gives the fluxes of interest, for example,

$$q_{\omega,1}^+ = 2\pi \int_0^1 I_\omega^+ \mu d\mu. \tag{D3}$$

Thus, the BTE in the forward direction is recast as

$$\frac{\partial q_{\omega,1}^+}{\partial t} + \beta v_\omega \frac{\partial q_{\omega,1}^+}{\partial x} = \frac{q_{\omega,1}^0 - q_{\omega,1}^+}{\tau_\omega}, \tag{D4}$$

where the coefficient β depends on the moment used ($\beta = 2/3$ here for $m = 1$). If we replace βv_ω by the effective 3D group velocity $v_{3D} = \beta v_\omega$, then Eq. (D4) is exactly the same as Eq. (A3) after the substitution $v_{1D} \rightarrow v_{3D}$. This v_{3D} involves an integration of the first moment over 2π steradians, causing it to differ from the bulk group velocity v_ω.

To obtain the solution in the backward direction, we also use energy conservation, the 3D version of Eq. (A18). The phonon energy density is

$$U_\omega = \eta \frac{q_{\omega,1}^+(x,t) + q_{\omega,1}^-(x,t)}{v_\omega}, \tag{D5}$$

where $\eta = 2$ arises from integrating I_ω with respect to the solid angle. Thus, with Eq. (D5), we can also solve the BTE in the negative direction using the same method in Appendix A and obtain the amplitude d_{3D} and phase shift ϕ_{3D} in the backward direction

$$\tan\phi_{3D} = \frac{2\beta\eta\omega_H\tau_\omega b}{(\beta\eta\omega_H\tau_\omega)^2 - a^2 - b^2} \tag{D6}$$

and

$$d_{3D} = -\frac{b}{(2\beta\eta\omega_H\tau_\omega + a)\sin\phi - b\cos\phi}. \tag{D7}$$

These general expressions can also be applied to the 1D case as we discussed before, such as the phase lag ψ_{gray} given by $\tan(\psi_{\text{gray}}) = -\frac{2d\sin\phi_{3D}}{1-d_{3D}^2}$. When $\beta = 1$ and $\eta = 1$, they exactly recover the 1D solution, as shown in Appendices A and B. The general expression for temperature in Eq. (B2), surface heat flux in Eq. (B5), phase lag in Eq. (B8), and apparent thermal conductivity in Eq. (4) all have the same forms except replace the 1D quantities v_{1D}, ϕ_{1D}, and d_{1D} with 3D quantities $v_{3D} = \beta v_\omega$, ϕ_{3D}, and d_{3D}. All the other parameters are the same.

[1] C. Dames and G. Chen, in *Thermoelectrics Handbook, Macro to Nano*, edited by D. M. Rowe (Taylor & Francis, New York, 2006), pp. 42-1–42-16.

[2] Y. K. Koh and D. G. Cahill, Phys. Rev. B **76**, 075207 (2007).

[3] S. G. Volz, Phys. Rev. Lett. **87**, 074301 (2001).

[4] Y. Ezzahri and K. Joulain, J. Appl. Phys. **112**, 083515 (2012).

[5] R. Venkatasubramanian, E. Siivola, T. Colpitts, and B. O'Quinn, Nature **413**, 597 (2001).

[6] I. Chowdhury, R. Prasher, K. Lofgreen, G. Chrysler, S. Narasimhan, R. Mahajan, D. Koester, R. Alley, and R. Venkatasubramanian, Nat. Nano. **4**, 235 (2009).

[7] A. I. Hochbaum, R. Chen, R. D. Delgado, W. Liang, E. C. Garnett, M. Najarian, A. Majumdar, and P. Yang, Nature **451**, 163 (2008).

[8] B. Poudel, Q. Hao, Y. Ma, Y. C. Lan, A. Minnich, B. Yu, X. Yan, D. Z. Wang, A. Muto, D. Vashaee, X. Y. Chen, J. M. Liu, M. S. Dresselhaus, G. Chen, and Z. F. Ren, Science **320**, 634 (2008).

[9] K. Hamad-Schifferli, J. J. Schwartz, A. T. Santos, S. Zhang, and J. M. Jacobson, Nature **415**, 152 (2002).

[10] A. S. Henry and G. Chen, J. Comput. Theor. Nanosci. **5**, 141 (2008).

[11] C. Bera, N. Mingo, and S. Volz, Phys. Rev. Lett. **104**, 115502 (2010).

[12] J. Garg, N. Bonini, B. Kozinsky, and N. Marzari, Phys. Rev. Lett. **106**, 045901 (2011).

[13] K. Esfarjani, G. Chen, and H. T. Stokes, Phys. Rev. B **84**, 085204 (2011).

[14] W. Li, N. Mingo, L. Lindsay, D. A. Broido, D. A. Stewart, and N. A. Katcho, Phys. Rev. B **85**, 195436 (2012).

[15] F. Yang and C. Dames, Phys. Rev. B **87**, 035437 (2013).

[16] A. J. Minnich, J. A. Johnson, A. J. Schmidt, K. Esfarjani, M. S. Dresselhaus, K. A. Nelson, and G. Chen, Phys. Rev. Lett. **107**, 095901 (2011).

[17] G. Pernot, H. Michel, B. Vermeersch, P. Burke, H. Lu, J.-M. Rampnoux, S. Dilhaire, Y. Ezzahri, A. Gossard, and A. Shakouri, *Symposium BB – Nanoscale Heat Transport–From Fundamentals to Devices*, MRS Proceedings (Materials Research Society, Pitusburg, 2011), Vol. 1347.

[18] K. T. Regner, D. P. Sellan, Z. Su, C. H. Amon, A. J. H. McGaughey, and J. A. Malen, Nat. Commun. **4**, 1640 (2013).

[19] J. A. Johnson, A. A. Maznev, J. Cuffe, J. K. Eliason, A. J. Minnich, T. Kehoe, C. M. Sotomayor Torres, G. Chen, and K. A. Nelson, Phys. Rev. Lett. **110**, 025901 (2013).

[20] A. J. Minnich, G. Chen, S. Mansoor, and B. S. Yilbas, Phys. Rev. B **84**, 235207 (2011).

[21] A. Minnich, Ph.D. Dissertation, MIT, 2011.

[22] G. Chen, J. Heat Tranfer **118**, 539 (1996).

[23] R. B. Wilson, J. P. Feser, G. T. Hohensee, and D. G. Cahill, Phys. Rev. B **88**, 144305 (2013).

[24] R. B. Wilson and D. G. Cahill, Nat. Commun. **5**, 5075 (2014).

[25] A. A. Maznev, J. A. Johnson, and K. A. Nelson, Phys. Rev. B **84**, 195206 (2011).

[26] A. J. Minnich, Phys. Rev. Lett. **109**, 205901 (2012).

[27] K. C. Collins, A. A. Maznev, Z. Tian, K. Esfarjani, K. A. Nelson, and G. Chen, J. Appl. Phys. **114**, 104302 (2013).

[28] C. Hua and A. J. Minnich, Phys. Rev. B **89**, 094302 (2014).

[29] K. T. Regner, A. J. H. McGaughey, and J. A. Malen, Phys. Rev. B **90**, 064302 (2014).

[30] A. Majumdar, J. Heat Transfer **115**, 7 (1993).

[31] M. F. Modest, *Radiative Heat Transfer*, 2nd ed. (Academic Press, San Diego, 2003), p. 456.

[32] R. A. Escobar, S. S. Ghai, M. S. Jhon, and C. H. Amon, Int. J. Heat Mass Transfer **49**, 97 (2006).

[33] F. Yang, T. Ikeda, G. J. Snyder, and C. Dames, J. Appl. Phys. **108**, 034310 (2010).

[34] A. A. Joshi and A. Majumdar, J. Appl. Phys. **74**, 31 (1993).

[35] C. Dames and G. Chen, J. Appl. Phys. **95**, 682 (2004).

[36] N. Mingo, L. Yang, D. Li, and A. Majumdar, Nano Lett. **3**, 1713 (2003).

[37] J. Callaway, Phys. Rev. **113**, 1046 (1959).

[38] J. M. Ziman, *Electrons and Phonons* (Oxford University Press, Oxford, 1960), p. 265.

[39] G. Chen, *Nanoscale Energy Transport and Conversion* (Oxford University Press, Oxford, 2005), p. 237.

[40] J. A. Malen, K. Baheti, T. Tong, Y. Zhao, J. A. Hudgings, and A. Majumdar, J. Heat Transfer **133**, 081601 (2011).

[41] D. G. Cahill, Rev. Sci. Instrum. **75**, 5119 (2004).

[42] W. H. Press, S. A. Teukolsky, W. T. Vetterling, and B. P. Flannery, *Numerical Recipes: The Art of Scientific Computing*, 3rd ed. (Cambridge University Press, Cambridge, 2007), p. 986.

[43] T. Bergman, A. Lavine, F. P. Incropera, and D. P. DeWitt, *Fundamentals of Heat and Mass Transfer*, 7th ed. (Wiley, Hoboken, NJ, 2011), p. 327.

[44] J. P. Dismukes, L. Ekstrom, E. F. Steigmeier, I. Kudman, and D. S. Beers, J. Appl. Phys. **35**, 2899 (1964).

[45] B. Abeles, Phys. Rev. **131**, 1906 (1963).

[46] E. S. Toberer, L. L. Baranowski, and C. Dames, Annu. Rev. Mater. Res. **42**, 179 (2012).

[47] Q. Hao, G. Chen, and M.-S. Jeng, J. Appl. Phys. **106**, 114321 (2009).

[48] L. Zeng and G. Chen, J. Appl. Phys. **116**, 064307 (2014).

[49] J. Y. Murthy, S. V. J. Narumanchi, J. A. Pascual-Gutierrez, T. Wang, C. Ni, and S. R. Mathur, Int. J. Multiscale Comp. Eng. **3**, 5 (2005).

[50] M. Greenberg, *Advanced Engineering Mathematics* (Prentice Hall, Upper Saddle River, NJ, 1998), p. 981.

[51] D. G. Cahill and R. O. Pohl, Annu. Rev. Phys. Chem. **39**, 93 (1988).

[52] D. D. Joseph and L. Preziosi, Rev. Mod. Phys. **61**, 41 (1989).

[53] E. Lifshitz, J. Phys. Ussr **8**, 110 (1944).

[54] L. Landau, J. Phys. Ussr **5**, 71 (1941).

[55] J. C. Ward and J. Wilks, Philos. Mag.7 **742**, 314 (1951).

[56] J. C. Ward and J. Wilks, Philos. Mag.7 **43**, 48 (1952).

[57] R. B. Dingle, Proc. Phys. Soc. London. A **65**, 374 (1952).

[58] C. C. Ackerman, B. Bertman, H. A. Fairbank, and R. A. Guyer, Phys. Rev. Lett. **16**, 789 (1966).

[59] H. E. Jackson and C. T. Walker, Phys. Rev. B **3**, 1428 (1971).

[60] S. J. Rogers, Phys. Rev. B **3**, 1440 (1971).

[61] A. Koreeda, R. Takanao, and S. Saikan, Phys. Rev. Lett. **99**, 265502 (2007).